

Article

Application of High-Resolution Aeromagnetic and Gamma-ray Spectrometry Surveys for Litho-Structural Mapping in Southwest China

Guixiang Liao^{1,2,3}, Yongbo Li^{1,2,3,4,*} , Yongzai Xi^{1,2,3,*} , Ning Lu^{1,2,3}  and Shan Wu^{1,2,3}

¹ Institute of Geophysical and Geochemical Exploration, Chinese Academy of Geological Sciences, Langfang 065000, China; lguixiang@mail.cgs.gov.cn (G.L.); luning@mail.cgs.gov.cn (N.L.); wshan@mail.cgs.gov.cn (S.W.)

² National Center of Geological Exploration Technology, Langfang 065000, China

³ Key Laboratory of Geophysical Electromagnetic Probing Technologies, Ministry of Natural Resources, Langfang 065000, China

⁴ Chinese Academy of Geological Sciences, Beijing 100037, China

* Correspondence: lyongbo@mail.cgs.gov.cn (Y.L.); xyongzai@mail.cgs.gov.cn (Y.X.)

Abstract: Airborne geophysical surveys serve as an effective tool for litho-structural mapping, providing extensive and high-resolution underground information. They offer vital data support for the interpretation and analysis of lithologies and structures, complementing surface geological mapping. In the study area of the Nanpanjiang-Youjiang metallogenic belt in southeast China, we obtained high-resolution aeromagnetic and gamma-ray spectrometry data covering an area of approximately 27,000 km², which facilitated the conduct of litho-structural mapping. The total magnetic intensity, reduction to the pole, and directional derivative maps generated from the aeromagnetic data, efficiently identified concealed rocks and faults. Additionally, the total count, potassium, thorium to potassium ratio, and ternary maps generated from the airborne gamma-ray spectrometry data demonstrated advantages in distinguishing carbonate rocks from clastic rocks. They also provided more comprehensive geological information, refining the structural strike and location interpreted by the aeromagnetic data. The litho-structural map produced in this study significantly contributes to our understanding of the structures in the Nanpanjiang area and offers valuable guidance for successful mineral exploration endeavors.

Keywords: airborne geophysical survey; aeromagnetic interpretation; gamma-ray spectrometry interpretation; lithologies and structures; Nanpanjiang area



Citation: Liao, G.; Li, Y.; Xi, Y.; Lu, N.; Wu, S. Application of High-Resolution Aeromagnetic and Gamma-ray Spectrometry Surveys for Litho-Structural Mapping in Southwest China. *Minerals* **2023**, *13*, 1424. <https://doi.org/10.3390/min13111424>

Academic Editor: Behnam Sadeghi

Received: 4 September 2023

Revised: 26 October 2023

Accepted: 7 November 2023

Published: 9 November 2023



Copyright: © 2023 by the authors. Licensee MDPI, Basel, Switzerland. This article is an open access article distributed under the terms and conditions of the Creative Commons Attribution (CC BY) license (<https://creativecommons.org/licenses/by/4.0/>).

1. Introduction

Airborne geophysical surveys are highly efficient exploration methods that overcome the challenges posed by surface surveys in difficult terrains, such as deserts, shallow covered areas, high mountains, and densely vegetated areas. They have found widespread application in geological surveys, mineral exploration, and environmental monitoring [1–6]. Litho-structural mapping forms the foundation for geological surveys and mineral exploration, aiding in the interpretation of lithologies, structures, and geological evolution [7–9]. By leveraging the petrophysical variations among different geological units, lithologies, and geological structures, airborne geophysical surveys offer a rapid approach for litho-structural mapping. They provide large-area, high-resolution underground information, which is crucial and beneficial for interpreting and analyzing lithologies and structures, thereby complementing surface geological mapping [10,11]. Processing and converting high-precision airborne geophysical data into various base maps and transformed maps facilitate the identification of detailed information about lithologies and geological structures, making geophysical interpretation more accessible.

The study area in this paper is located in the Nanpanjiang-Youjiang metallogenic belt in China (Figure 1), renowned as the “Golden Triangle” area. This region is well-known for its significant mineral deposits, including gold, lead-zinc, and manganese. Furthermore, it is recognized as a concentrated area of Carlin-type gold mines [12,13]. Encompassing an approximate area of 27,000 km², the study area is characterized by diverse terrain, complex landforms, and high elevations, with a northwest to southeast trend. In this particular area, a limited 1:200,000 scale aeromagnetic survey was conducted during the 1960s. However, since then, there has been a significant lack of systematic and high-precision airborne geophysical surveys at larger scales. Consequently, there is a pressing need for enhanced regional fundamental geological research in this area. Between 2015 and 2018, we conducted a helicopter-borne geophysical survey at a scale of 1:50,000, acquired high-resolution magnetic and gamma-ray spectrometry data, and performed litho-structural mapping. Compared to previous studies, our work not only possesses higher accuracy but also better caters to the requirements of geological exploration and mineral prospecting.

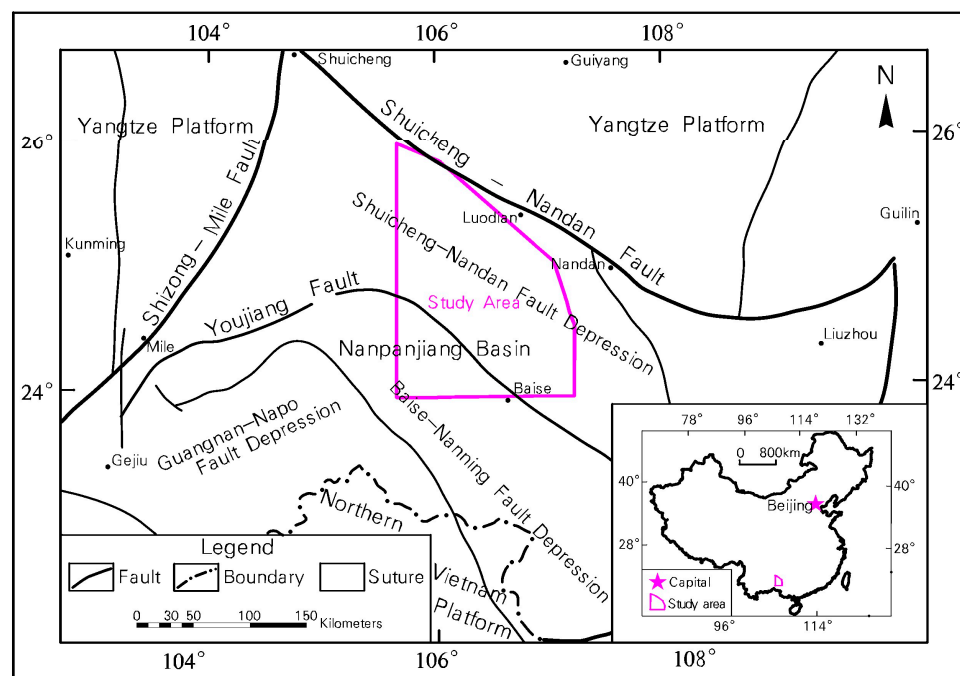


Figure 1. Regional structure map of the Nanpanjiang-Youjiang metallogenic belt (modified from reference [12]). The purple polygon represents the study area.

Aeromagnetic surveys assist in identifying rock bodies with different magnetization and regional faults, while also providing insights into the depth of underlying bedrock [14–16]. Airborne gamma-ray spectrometry surveys capture natural gamma emissions emitted by the natural radiogenic elements: potassium (K), thorium (Th), and uranium (U), present on the Earth’s surface, which provides valuable geophysical and geochemical information related to mineralization. It is particularly effective in distinguishing different lithologies and accurately characterizing geological units. Therefore, it has been widely employed in geological mapping and often complements aeromagnetic survey [17–22]. In this study, we utilized high-precision aeromagnetic and gamma-ray spectrometry data, in conjunction with geological information, to conduct a comprehensive analysis of the structural distribution, stratigraphy, and distribution characteristics of igneous rocks in the study area. The findings of this study could serve as valuable references for fundamental geological research and mineral exploration in the Nanpanjiang-Youjiang metallogenic belt.

2. Geological Setting

The Nanpanjiang-Youjiang metallogenic belt possesses favorable geological conditions and abundant mineral resources, showcasing immense potential for mineral exploration [12,13]. It has been officially recognized as a national key metallogenic belt in China since 2013. The study area covers the eastern section of the Nanpanjiang-Youjiang metallogenic belt and is situated at the intersection of Guizhou, Guangxi, and Yunnan provinces (Figure 1).

The study area is situated within the tectonic framework of the Nanpanjiang basin, specifically known as the Youjiang Rift-foreland basin, Youjiang basin, Youjiang regenerated geosyncline, or Youjiang Orogenic belt. It is located in the Shuicheng-Nandan fault depression zone and the Baise-Nanning fault depression zone, as depicted in Figure 1. The study area exhibits well-developed fold structures, including the large-scale Leye “S”-shaped anticline, Tian’e anticline, Laizishan anticline, Lingyun twisting anticline, and Yueli syncline. Additionally, the area is influenced by the Dongwu movement, resulting in dome structures in the area, such as uplifts or domes, including the Longchuan dome. The major faults in the area consist of the northwest-trending Youjiang fault, Ziyun-Donglan fault, northeast-trending Luodian-Guangnan fault, Wangmo-Bama fault, nearly south-north trending Puding-Zhenfeng fault, nearly east-west trending Nihan fault, and Tianlin-Bama fault.

The study area displays a diverse stratigraphic development, encompassing exposures ranging from the Paleozoic to the Neogene system. The most widely distributed system is the Mesozoic Triassic, as shown in Figure 2. The Cambrian system primarily comprises marine shale and dolomite and is only exposed in the southwestern part of the study area. The Ordovician and Silurian systems are absent. From the late Early Devonian to the Early Triassic system, the Nanpanjiang-Youjiang area witnessed the development of typical carbonate platforms and deep-water basin sedimentary. The platform facies area is characterized by sedimentary carbonates, biogenic reef limestones, mud-crystal limestones, oolitic limestones, and conglomerates. In contrast, the basin facies area is dominated by deep-water sediments, such as mudstone and chert. The Youjiang basin exhibits extensive Middle and Lower Triassic turbidite clastic rock deposits, reaching a thickness of up to 6000 m. The Upper Triassic series are sporadically distributed in the basin, characterized by clastic rock deposition. The Jurassic and Cretaceous systems have limited outcrops, primarily composed of sandstones. The Tertiary and Quaternary systems are predominantly characterized by fluvial and lacustrine deposits, distributed in river terraces and floodplains.

The development of magmatic rocks in the study area is generally moderate. Intrusive bodies are mainly distributed in the Longchuan, Yufeng, Bo’ai-Yangxu, and Sanglang-Luodian areas. These bodies are primarily composed of basaltic andesite, with occasional occurrences of ultrabasic to intermediate-acidic dikes. The distribution direction of rock belts in the Bo’ai-Yangxu area is prominently controlled by northwest and east-west trending faults, with rock bodies directly occurring in fault fracture zones. The extrusive basalt is found in the Longchuan, Yufeng, and Bo’ai-Yangxu areas, forming thin annular and layered rock formations influenced by the Dongwu movement.

The Himalayan movement has caused continuous uplift of the crust in the study area, resulting in erosion and weathering of the strata. Rivers have carved through the area, creating high peaks and deep valleys with typical karst landforms, as shown in Figure 3. The terrain in this area is highly undulating, making surface surveys challenging. Therefore, in this study, an airborne geophysical survey was employed to investigate the distribution of deep fault structures and magmatic rocks in this area.

Based on the petrophysical survey conducted in this study area, we present the petrophysical parameters of magnetic susceptibility and gamma-ray spectrometry in Tables 1 and 2, respectively. Table 1 reveals that diabase exhibits the strongest magnetic characteristics, leading to strong magnetic anomalies, while sedimentary rocks generally display weak magnetism, corresponding to a stable weak magnetic field. From Table 2, it is evident that intermediate rocks and acidic rocks exhibit high radioactivity, resulting in significant gamma-ray spectral anomalies. In contrast, sedimentary rocks and mafic rocks show low radioactivity, leading

to relatively low gamma-ray spectral anomalies. Moreover, the radioactive content of volcanic rocks and clastic rocks varies widely and is associated with their composition. These petrophysical parameters can serve as the basis for interpreting airborne geophysical data in this area.

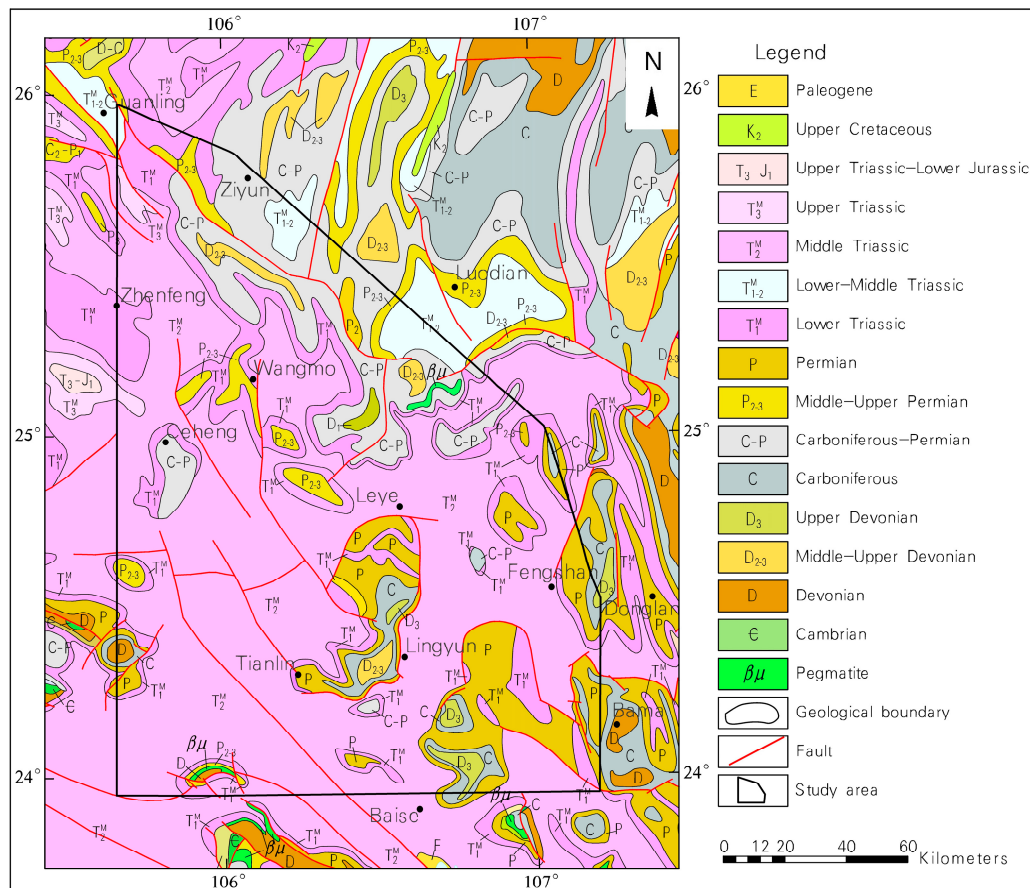


Figure 2. Geological schematic map of the study area (modified from the geological map with a scale of 1:500,000). The black polygon represents the study area.

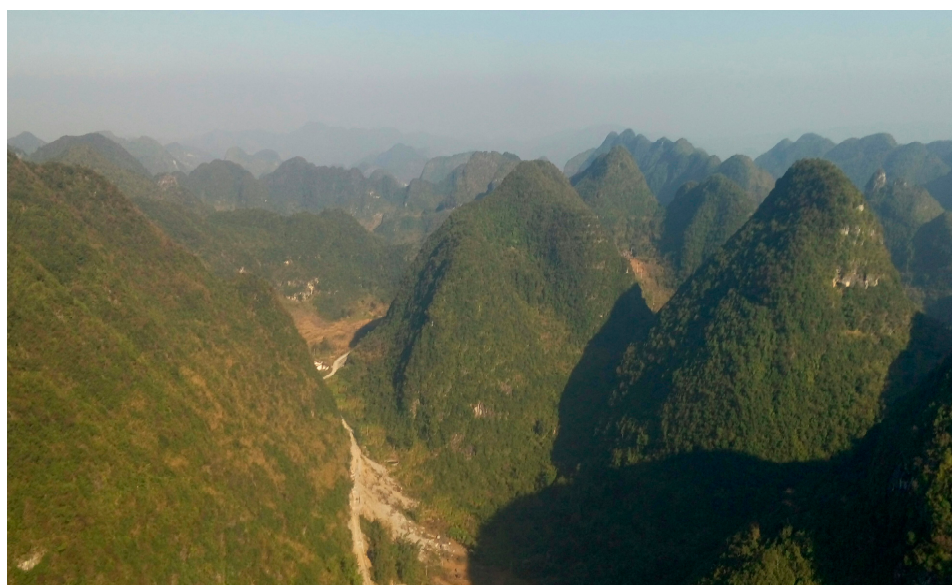


Figure 3. The typical karst landform of the study area.

Table 1. Magnetic susceptibility (10^{-6} SI) parameter of strata and rocks in the study area.

No.	System	Measured Points Number	Min	Max	Mean
1	Q	9	111.6	853.3	327.2
2	T ₃	6	38.3	90.0	59.4
3	T ₂	321	−10.0	361.6	155.0
4	T ₁	12	0.0	196.6	84.2
5	P ₂	30	−31.7	166.7	28.7
6	P ₁	79	−43.3	716.6	13.2
7	C	53	−58.3	43.3	6.3
8	D	15	−16.7	23.3	6.9
9	diabase	11	566.6	23,666.7	4458.9

Table 2. Gamma-ray spectrometry parameter of rocks in the study area.

No.	Rock	Total Count (Ur)	U (ppm)	Th (ppm)	K (%)
1	granite	38.23	4.15	25.08	4.90
2	diorite	27.20	4.22	16.57	3.12
3	gabbro	12.10	0.66	7.63	1.60
4	ultrabasic	12.78	1.94	6.56	1.70
5	tuff	37.43	1.60	17.06	6.18
6	quartz schist	15.03	0.69	9.86	1.96
7	marble	15.50	2.68	7.11	1.96
8	limestone	10.45	1.27	4.85	1.39
9	sandstone	13.73	3.29	5.02	1.65
10	conglomerate	14.58	1.55	5.50	2.06
11	mudstone	24.63	0.26	13.35	3.82

3. Methodology

3.1. Data Collection

The airborne geophysical survey system used in this study consists of two measurement subsystems: a total magnetic field measurement subsystem and a 256-channel gamma-ray spectrometry measurement subsystem, as shown in Figure 4. This system allows for the simultaneous recording of total magnetic intensity (TMI), gamma-ray spectrometry, and position data. It integrates a magnetometer, gamma-ray spectrometer, radar altimeter, global positioning system (GPS) receiver, and navigation system on an Airbus AS350–B1 helicopter (Airbus Group, Toulouse, France). The magnetometer is mounted on a probe extending approximately 4 m in front of the helicopter, while the gamma-ray spectrometer is installed inside the helicopter cabin. The sampling rates for TMI and gamma-ray spectrometry measurements are 10 Hz and 1 Hz, respectively.

A 1:50,000-scale airborne geophysical survey was conducted between 2015 and 2018. A total of 54,660 line-kilometers of aeromagnetic and gamma-ray spectrometry data were collected along the SN direction, with a line spacing of 500 m (Figure 5). The average flight height was 150.5 m, and the average cross-track offset was 9.6 m. The dynamic noise of the aeromagnetic data ranged from 16.71 to 15.87 pT, while the static noise of the magnetic diurnal variation ranged from 0.97 to 3.81 pT. The resolution of the airborne gamma-ray spectrometry, using a NaI crystal (¹³⁷Cs), ranged from 7.7% to 11.2%.

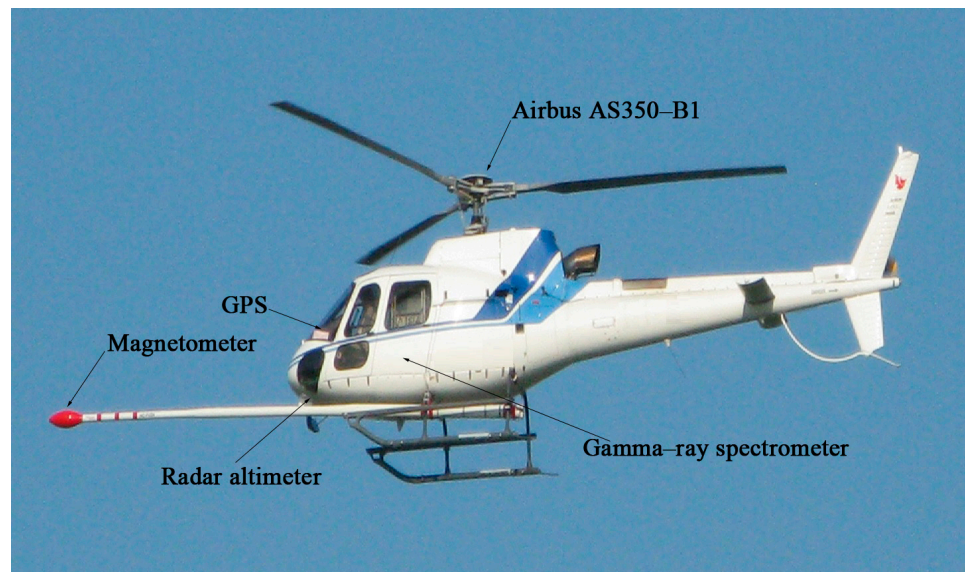


Figure 4. The airborne geophysical survey system.

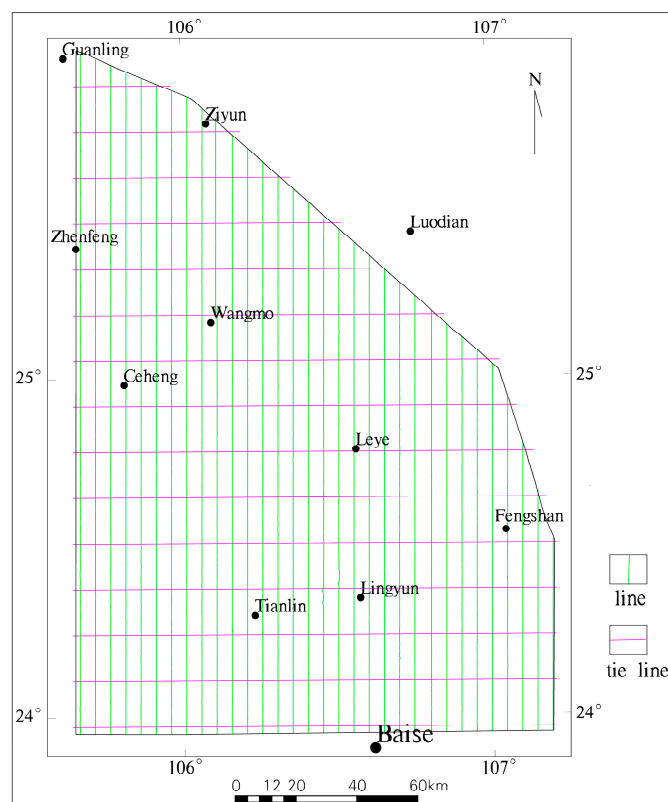


Figure 5. Schematic map of measurement lines in the study area. The green lines represent the measurement lines in the north-south direction, displayed every 10 measurement lines. The purple lines represent the cutting lines in the east-west direction, with a spacing of 15 km.

3.2. Data Processing

We primarily utilized the software Oasis Montaj [23,24] (Geosoft Inc., Toronto, ON, Canada) to process the airborne geophysical data, as it is well-suited for handling and visualizing extensive geophysical datasets. Preprocessing was performed on the raw data obtained from aeromagnetic and gamma-ray spectrometry surveys, which involved standard leveling and necessary corrections, such as airplane background correction, cos-

mic rays background correction, Compton scattering correction, air radon background correction, and height correction. Gridding of the data was accomplished using the minimum curvature algorithm with a cell size of 250 m (i.e., 1/2 of the line spacing) [25]. All maps presented in this paper were georeferenced to the China geodetic coordinate system 2000 (CGCS2000) in Zone 18 of the Northern Hemisphere (UTM Z18N).

The processing of aeromagnetic data generally involve transformations and filtering techniques, such as reduction to the pole (RTP), continuation, and derivatives [26–35]. In this study, several signal enhancement techniques were implemented. Firstly, considering the inclination and declination of the ambient magnetic field in the center of the study area (38.38° and -1.93° , respectively), the RTP transformation (Figure 6b) was performed to convert the bipolar magnetic anomaly into a positive anomaly centered on the causative source [36,37]. Secondly, the upward continuation transformation (Figure 6c) was applied to the magnetic data to suppress the magnetic field caused by shallow and small geological bodies while highlighting the magnetic field caused by larger geological bodies. This technique is particularly useful for emphasizing deep structures such as major fractures and concealed rocks. Thirdly, the vertical derivative filter was employed to enhance localized anomalies, emphasizing short-wavelength anomalies and reducing long-wavelength anomalies associated with deep sources. The vertical derivative filter helps distinguish closely spaced short-wavelength anomalies. In addition, the directional derivative filter was primarily applied to highlight the locations of fractures and vein rocks that strike perpendicular to the derivative’s direction, as well as the boundary lines of large-scale geological bodies (Figure 6d). It is also used to enhance magnetic anomalies along specific directions, especially at 45° , 90° , 135° , and 180° . In this study, the derivative maps were generated in the direction of 45° (Figure 7a) and 135° (Figure 7b), primarily to determine the location and strike of faults.

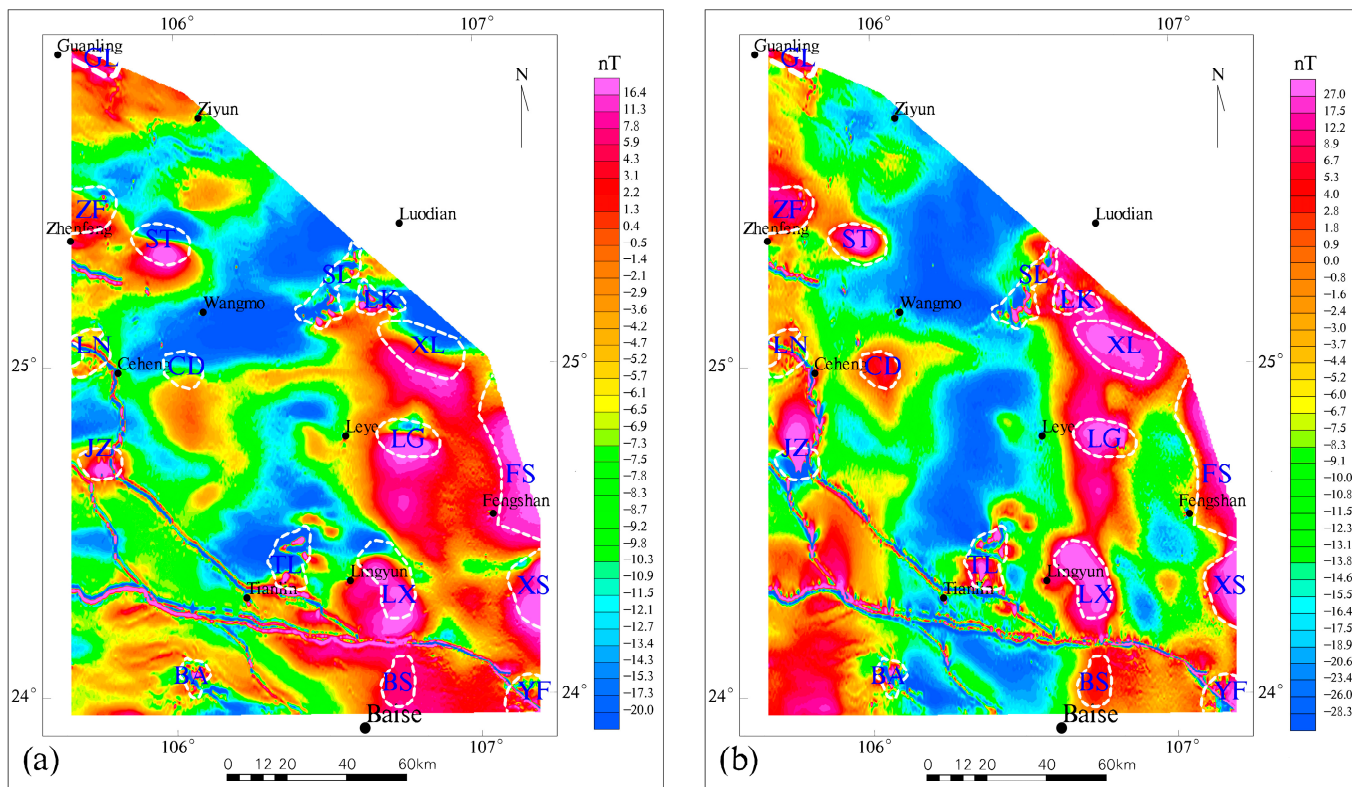


Figure 6. Cont.

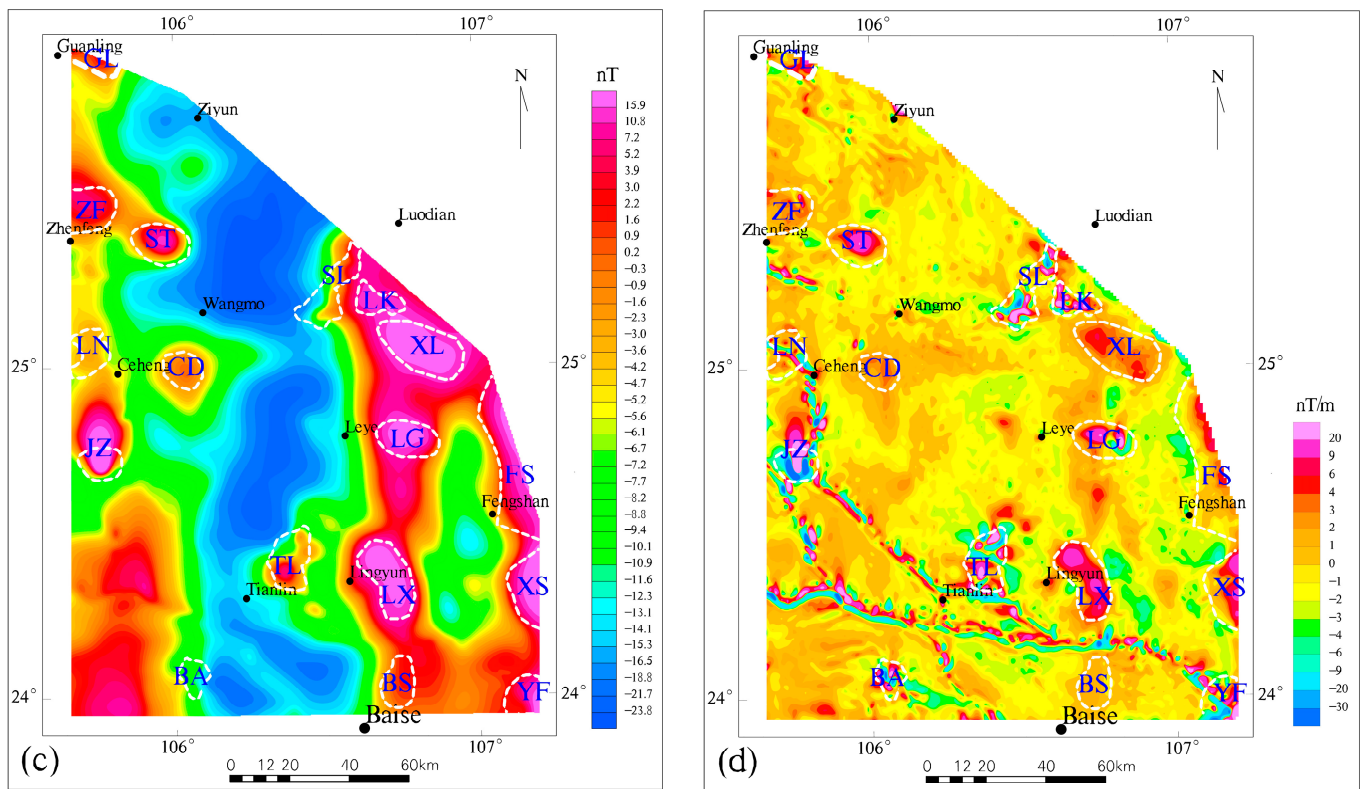


Figure 6. The concealed rocks interpretation map from (a) TMI map after IGRF, (b) RTP map, (c) upward continuation to 3.0 km map, and (d) first vertical derivative map. The white polygon represents the inferred concealed rock, named in blue color.

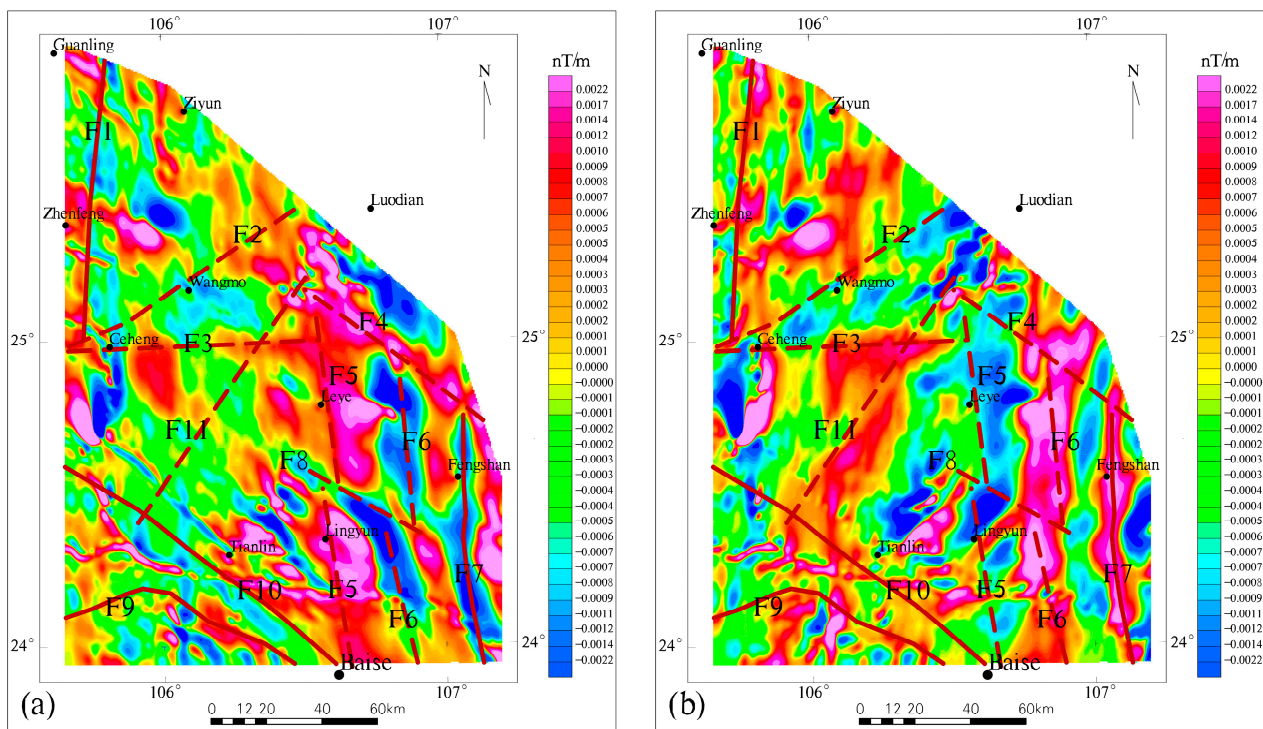


Figure 7. The faults interpretation map form (a) 45° and (b) 135° directional derivative maps. The red solid line represents the current fault, and the red dotted line represents the inferred fault.

Gamma-ray spectrometry surveys measure the gamma radiation emitted by three natural radioactive elements: K, Th, and U near the Earth's surface. It serves as an effective method for identifying lithologies and geological contacts in geological mapping, often used as a supplement to aeromagnetic survey. The processing of gamma-ray spectrometry data is crucial for effectively utilizing relevant mineralization information and suppressing interference. This process typically involves multiple steps to correct for the interactions and attenuation of gamma rays as they travel from the source through the air to the detectors on the helicopter. In this study, the processing of gamma-ray spectrometry data included corrections for aircraft background, atmospheric radon, and flight altitude to ensure accurate and reliable interpretations. To effectively identify lithologies and radioactive anomalies, enhancement operations were performed, including total count, K concentration, Th to K ratio (Th/K), and ternary composition maps. These enhancement maps can be correlated with the trends and patterns of geological units for accurate geological mapping.

4. Results and Discussions

4.1. Aeromagnetic Interpretations

Based on the TMI, RTP, upward continuation, and vertical and directional derivative maps, we have interpreted the concealed rocks and faults, as illustrated in Figures 6 and 7. Figure 6a,b depicts the TMI map after IGRF, indicating the response of the thicker weakly magnetic sedimentary layers as a weak magnetic field. The RTP map demonstrates a notable northward shift in the center of the magnetic anomalies. The regional magnetic field exhibits a general pattern of gradually strengthening from west to east and from north to south, with distinct variations in magnetic background and magnetic anomaly characteristics at the local level. A comparison of these two maps reveals a noticeable northward shift in the magnetic anomaly centers following RTP transformation. In particular, the XL anomaly center shows the most significant movement, shifting approximately 7 km to the north. In Figure 6, the code names, such as XL, CD, etc., represent the hidden rocks inferred by the aeromagnetic maps.

According to the distribution of magmatic rocks and faults, hidden rock bodies in the study area were identified and qualitatively interpreted using the TMI after IGRF, RTP, upward continuation to 3.0 km, and first-order derivative maps (Figure 6). Figure 6c,d clearly display distinct characteristics of most hidden rock bodies, enabling the direct determination of their boundaries. Specifically, the boundaries of CD, LX, LG, and ST coincide with magnetic anomaly boundaries. The ZF, CD, XL, LG, LX, FS, and XS exhibit low and gradually changing magnetic anomaly patterns. Since no exposed magmatic rocks have been found in these areas, it can be inferred that these anomalies are caused by concealed rock bodies. Furthermore, based on the morphological characteristics of the magnetic anomalies, it is inferred that they are associated with deep intermediate-acidic rock bodies. On the other hand, SL, LK, TL, BA, and YF display chaotic magnetic anomaly features with higher intensity and steeper gradients. These areas are associated with outcrops of diabase veins, indicating that the magnetic anomalies in these areas are caused by shallow diabase rocks.

The interpretation of faults based on aeromagnetic data typically involves analyzing various magnetic field zones, magnetic field gradient zones, linear anomaly zones, beaded anomaly zones, anomaly truncation zones, anomaly uplift zones, and anomaly dislocation zones. However, due to the influence of thick non-magnetic sedimentary layers, most of the fault structures in the study area do not exhibit distinct features in the aeromagnetic maps (Figure 6). Therefore, in this study, the identification of faults primarily relies on the directional derivative maps, as shown in Figure 7. It is important to note that F1, F7, F9, and F10 in Figure 7 correspond to actual geological features. Fault F1 approximately trends in the north-south direction and serves as a boundary between different tectonic zones. Its western side corresponds to the southwestern Qiannan depression, while the eastern side corresponds to the Nanpanjiang depression [38]. Specifically, in Figures 6b and 7a, Fault

F1 is depicted as a boundary between different magnetic fields, with a higher magnetic field on the western side. This is further illustrated in Figure 7, particularly in Figure 7b, where it represents a discontinuous magnetic anomaly zone. Fault F10, also known as the Youjiang fault, acts as the boundary between different tectonic zones. Its southwestern side corresponds to the Baise-Nanning rift basin, while the northeastern side corresponds to the Ziyun-Nandan rift basin [39]. Figure 6a exhibits distinct characteristics, with arc-shaped magnetic anomalies on the southwestern side predominantly oriented east-west, while the magnetic anomalies on the opposite side mainly trend northwest-southeast and northeast-southwest.

In Figure 6a, it is evident that the magnetic anomalies in the eastern part of the study area are significantly higher than those in the western part, indicating a shallower magnetic basement in the east. There is a Fault F5, which trends approximately north-south and divides the study area into eastern and western blocks. Figure 7a illustrates that Fault F5 is segmented into southern and northern segments by the later northeastward Fault F8. The existence of Fault F8 is also supported by evidence from Figure 2. Furthermore, it is important to note that linear anomalies with high intensity and steep gradients are observed throughout the entire study area, spanning from southeast to northwest. These anomalies are particularly prominent in areas such as the Yufeng–Tianlin–Ceheng area, the Longchuan–Ding’an area, and the Yangxu–Pingshu area. These anomalies are attributed to the presence of artificial high-voltage DC power lines. The magnetic field characteristics mentioned above are comprehensive reflections of various structures, magmatic activities, strata, and lithologic distributions, forming the basis for litho-structural mapping.

4.2. Gamma-Ray Spectrometry Interpretation

After conducting a thorough analysis of the gamma-ray spectrometry characteristics of various geological strata in the study area, we performed a statistical analysis using the geological data. As a result, we established interpretation criteria for stratigraphic division, which are presented in Table 3. We eliminated biased data that was potentially caused by flight altitude errors and local anomalies while retaining the majority of the data points with minimal differences. These data points represent approximately 80% of the data points within the geological units.

Table 3. Statistical results of airborne gamma-ray spectrum content in the study area.

No.	System	K (%)		U (ppm)		Th (ppm)	
		Min	Max	Min	Max	Min	Max
1	E	0.50	0.83	1.78	2.43	5.80	7.97
2	K	0.33	0.61	1.83	2.18	5.43	6.92
3	T ₃	1.23	1.36	2.28	2.66	10.21	10.91
4	T ₂	1.01	1.21	2.16	2.65	8.28	9.41
5	T ₁₋₂	0.50	0.64	3.35	4.69	5.53	7.18
6	T ₁	0.85	1.13	2.49	3.01	7.47	8.71
7	P ₂	0.44	0.74	2.73	3.46	5.92	7.45
8	P ₁	0.39	0.68	2.01	2.50	4.89	6.49
9	P ₁₋₂	0.67	0.89	1.91	2.41	7.17	8.41
10	C ₁ –P ₁	0.19	0.28	1.35	1.78	3.09	3.94
11	C–P	0.31	0.47	1.40	1.80	4.26	5.44
12	C ₂	0.18	0.28	1.51	2.04	3.29	4.26
13	C	0.46	0.69	2.25	2.97	5.26	6.54
14	C ₁	0.29	0.47	1.56	2.05	4.21	5.58
15	D ₃	0.33	0.59	1.66	2.19	4.02	5.40
16	D ₂	0.76	1.12	2.02	2.55	7.02	8.89
17	D ₁₋₂	1.02	1.25	2.63	3.15	8.03	9.37
18	D	0.59	0.96	2.57	3.31	5.31	7.15
19	D ₁	1.24	1.58	3.01	3.68	8.91	10.60
20	€	1.57	1.86	3.76	4.38	7.92	9.19

The study area predominantly consists of carbonate rocks and clastic rocks. Figure 8 illustrates the gamma-ray spectrometry maps of this area, revealing significant differences in radioactive characteristics between carbonate rocks and clastic rocks. In this figure, code names such as CZ, LY, LZ, FB, LF, LL, and BO represent different sedimentary environments. The Triassic system is extensively distributed and exhibits significantly lower radioactive isotope content in carbonate rock deposited in the platform environment compared to clastic rock deposits. The Devonian, Carboniferous, and Permian systems are primarily composed of carbonate rocks, with minimal differences observed between the homologous sedimentary strata.

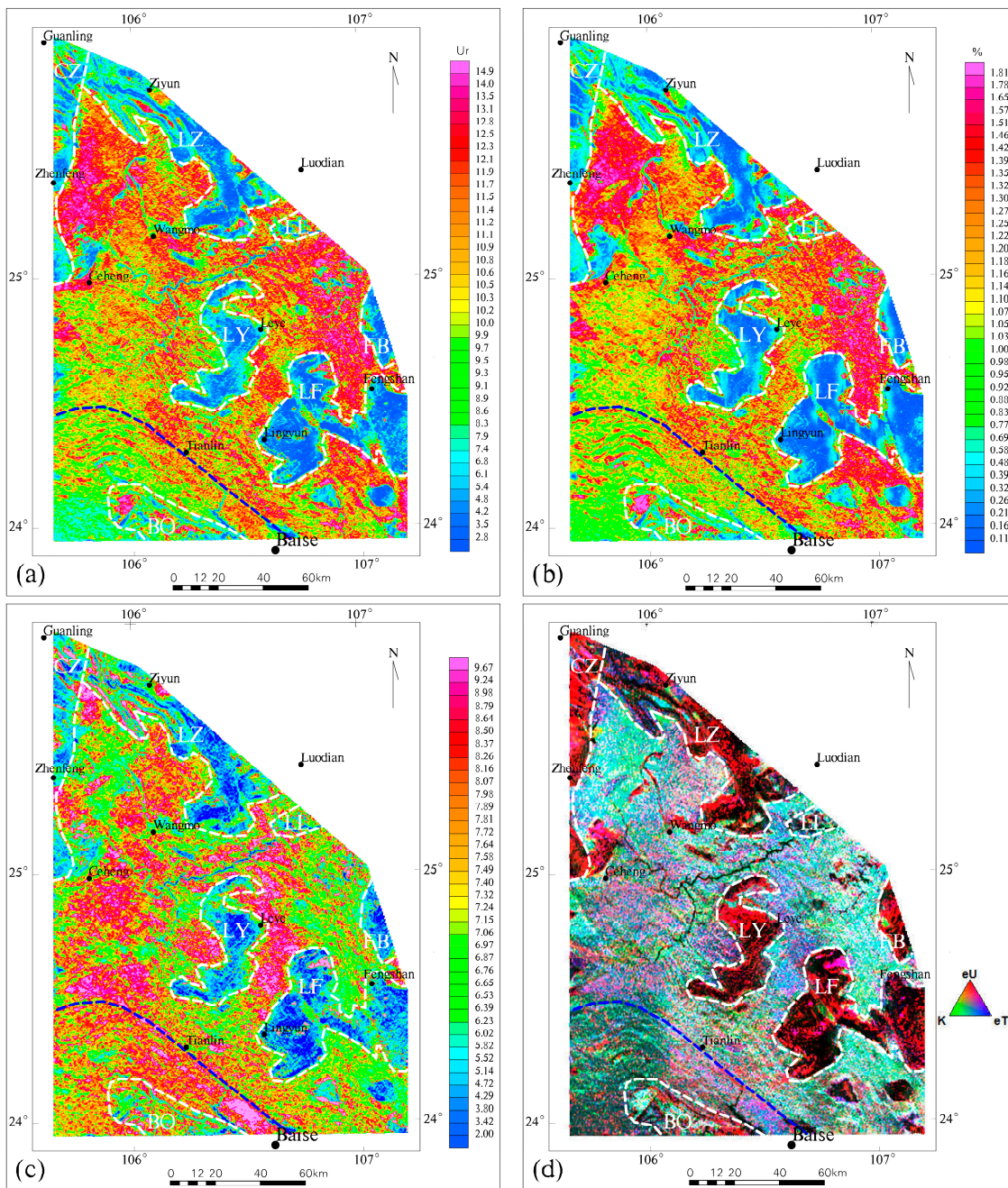


Figure 8. Gamma-ray spectrometry maps. (a) Total count map, (b) K concentration map, (c) Th/K map, and (d) red-green-blue ternary composition map of the three radiogenic elements: U, K, and Th. The white polygon represents the different sedimentary environments named in white color, and the blue dashed line represents the boundary between different gamma-ray spectrometry fields.

In the study area, the Triassic system is extensively distributed, and its gamma-ray spectral characteristics are strongly influenced by regional tectonics. In Figure 8, CZ represents a stable platform area characterized by the presence of platform-type carbonate rocks, exhibiting a low background gamma-ray spectrum. Based on the regional geological survey, CZ can be further divided into the Upper, Middle, and Lower Triassic series. In the eastern part of CZ, the Nanpanjiang area is a subsidence tectonic unit characterized by the development of basin-type clastic rocks with high K and Th contents. Some scholars suggest that the Nanpanjiang area contains sedimentary deposits of several kilometers of turbidites, which are inferred to be Middle Triassic clastic rocks (turbidites) [40], such as the Triassic system surrounding Tianlin and Wangmo.

The LY, LZ, FB, and LF areas all display tight-fold structures predominantly composed of the Paleozoic system, which are depicted as blue areas in Figure 8a–c, aligning well with the geological map. These areas are also represented as black and red areas in the red-green-blue ternary composition map (Figure 8d). Based on the geological map, it can be inferred that they all reflect the carbonate sedimentary strata. The K and Th contents present different ranges of variation within the Paleozoic formations. Specifically, the K contents range from 0.33% to 0.96% in the Devonian system, 0.18% to 0.69% in the Carboniferous system, and 0.26% to 0.74% in the Permian system. As for the Th contents, they range from 4.02 ppm to 7.15 ppm in the Devonian system, 3.29 ppm to 6.54 ppm in the Carboniferous system, and 4.36 ppm to 6.49 ppm in the Permian system.

In localized areas within the LL and BO regions, there are outcrops of diabase dykes with low K and Th contents. The K content ranges from 0.32% to 0.74%, while the Th content ranges from 4.36 ppm to 6.96 ppm. The magnetic field map and the diabase boundary in the geological map were both considered to determine the extent of the diabase. The ternary map reveals a distinct gamma-ray spectrometry boundary line approximately 10 km northeast of Baise, extending westward from Tianlin, denoted by the blue dashed line in Figure 8d. This line exhibits a pronounced arc-shaped feature in the southern region, which is not observed in the northern region. The proximity of this blue dashed line to Fault F10 suggests that it reflects the gamma-ray spectral characteristics of this fault in gamma-ray spectrometry maps.

4.3. Litho-Structural Map

Based on the interpretation of various aeromagnetic and airborne gamma-ray spectrometry maps (Figures 6–8), we have mapped the lithologies and structures of the study area, as shown in Figure 9. The key findings can be summarized as follows:

- (1) The Neogene system is limited to a small area, with the total gamma-ray spectrometry count ranging from approximately 1.91 Ur to 8.8 Ur. It is primarily exposed in small areas along the Youjiang river in the Baise basin and at the edges of the Leye “S”-shaped structure, i.e., the LY in Figure 8. The Youjiang area exposes the Paleogene Eocene series, mainly consisting of clastic rocks in the rift basin, while the Leye area exposes the Quaternary system.
- (2) Triassic turbidite, deposited in deep-sea basins, is widely distributed in the Nanpanjiang basin and exhibits a high gamma-ray spectrum. On the other hand, the Triassic turbidite deposited in shallow marine-slope environments is predominantly found within the Dian-Dongnan fold belt in the southwestern part of the study area, characterized by a low gamma-ray spectrum. Triassic carbonate rocks, deposited in platform environments, are mainly distributed on the western side of Fault F1, showing a low gamma-ray spectrum. Furthermore, gamma-ray spectrometry allows for the identification of different sedimentary source rocks within the Triassic strata, providing additional details for the geological map.
- (3) The main components of isolated platform-type anticlinal fold structures in the study area are the Permian, Carboniferous, and Devonian systems. These structures are predominantly composed of carbonate rocks, with clastic rocks as a secondary component. The gamma-ray spectral fields generally exhibit low values, although some localized

areas show high values. In the areas where carbonate rock was deposited within the anticlinal folds, certain regions are identified as clastic rock areas. For example, in Figure 8, the LZ area shows high gamma-ray spectrometry in the Upper Devonian series, indicating the presence of terrigenous clastic rocks. Additionally, within these delineated carbonate anticline folds, different sedimentary source rocks can be identified in some areas, which provides further refinement to the geological map.

- (4) The Cambrian system has a limited outcrop area and represents the oldest exposed strata in the study area. The gamma-ray spectral characteristics of the total count and K contents between the exposed Cambrian system and the overlying Devonian system are very similar. However, their Th contents differ significantly, particularly in terms of Th/K, which is characterized by low gamma-ray spectrometry in Figure 8c.
- (5) Based on the analysis of the aeromagnetic field characteristics and known fault structures, we have classified the fault structures identified through aeromagnetic data. The study area exhibits distinct linear structural zones: the faults trending north-south and nearly north-south are predominantly distributed in the eastern part of the study area, while the faults trending east-west and nearly east-west are primarily found in the central and southern parts. The northeast-trending faults are mainly concentrated in the western part, and the arc-shaped faults are mainly located along the south-western boundary, aligning with the regional tectonic framework. It is important to note that some faults inferred from the aeromagnetic data are refined using the gamma-ray spectrometry data, specifically for Faults F1 and F10. The gamma-ray spectral characteristics of Fault F1 reveal additional details in Figure 8, particularly the presence of discontinuities in the southern Zhengfeng area. This correction was also applied to Fault F10. As a result, the final strike and position of Faults F1 and F10 in Figure 9 differ from those in Figure 7, representing corrections and additions to the geological map.

Airborne geophysical surveys are undoubtedly a rapid means of acquiring regional geophysical field information over vast areas. However, they do have certain limitations. For instance, the inferred concealed rock bodies derived from aeromagnetic data in this study lack depth information, as aeromagnetic data represents a comprehensive reflection of all subsurface magnetic bodies. To address this issue, aeromagnetic inversion based on drilling and petrophysical data is required. On the other hand, airborne gamma-ray spectrometry data can effectively distinguish various surface rocks, making it a valuable method for lithological mapping. Nevertheless, the measured radioactive element content only provides an average within a specific range on the Earth's surface, making it challenging to precisely delineate the boundaries between different rocks. Consequently, the litho-structural map obtained in this study (Figure 9) serves as a confirmation and supplement to the existing geological map, rather than a substitute for surface geological mapping. In the future, it would be advantageous to combine additional petrophysical surveys and geological investigations to mutually complement and enhance both the litho-structural map and the geological map.

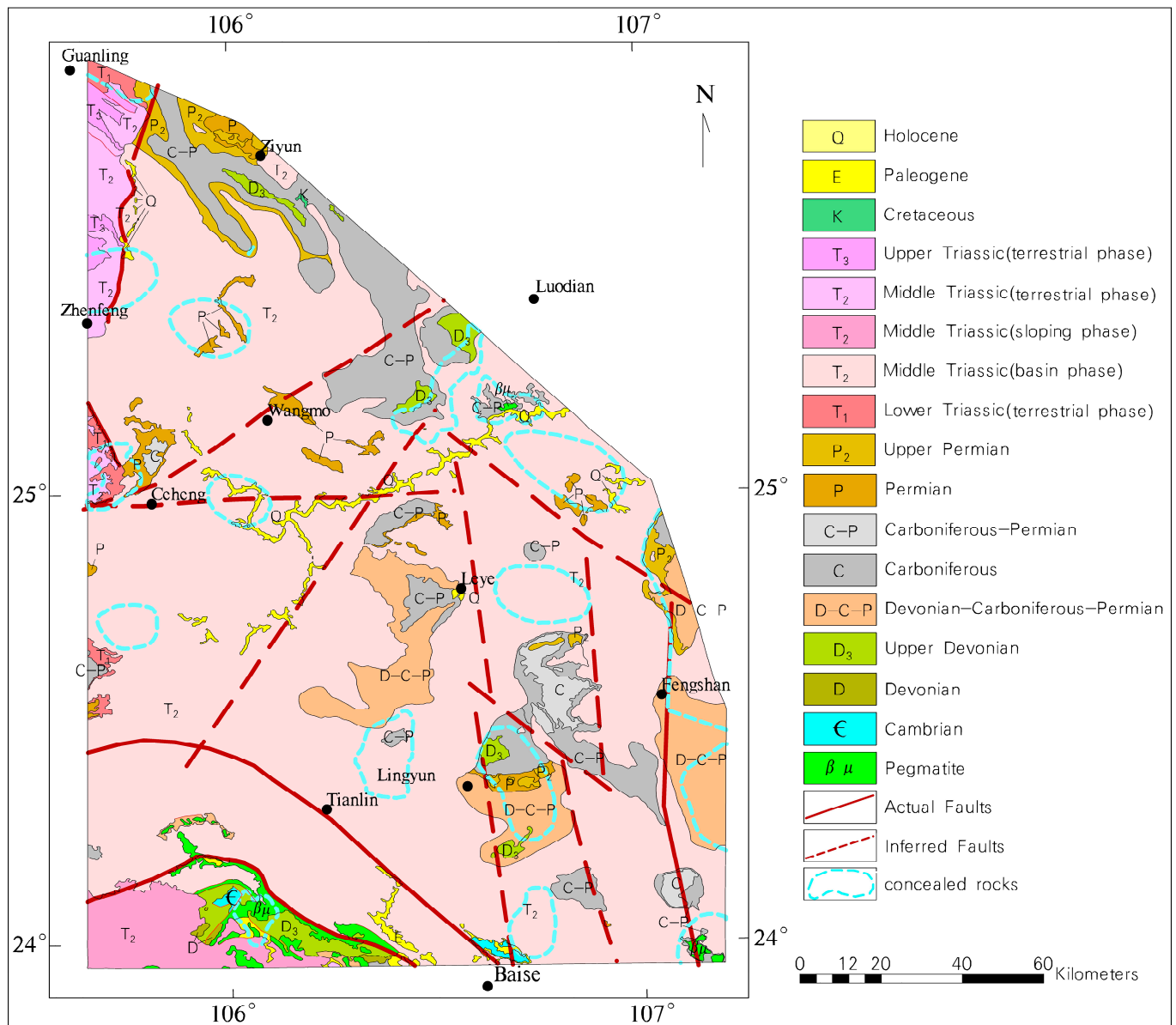


Figure 9. Litho-structural map inferred by airborne geophysical survey. The light blue circle represents the concealed rock, and the dark red solid line represents the actual fault, the dark red dash line represents the inferred fault.

5. Conclusions

Through the processing and joint interpretation of aeromagnetic and gamma-ray spectrometry data, we have successfully mapped the lithologies and structures in the study area, significantly improving the original geological map. The magnetic anomalies in the TMI map after IGRF exhibit a noticeable northward shift after RTP transformation, which provides reliable evidence for delineating the central location of the concealed rock bodies. Based on the aeromagnetic data, we have delineated 17 concealed rock bodies (Figure 6) and inferred the presence of 11 faults (Figure 7). The airborne gamma-ray spectrometry data has proven to be highly effective in distinguishing stratigraphic lithologies within different sedimentary environments. The majority of the carbonate rocks deposited in platform facies present a low gamma-ray spectrum (Figure 8), while most of the clastic rocks deposited in marine facies tend to display a high gamma-ray spectrum. Furthermore, the gamma-ray spectrometry data has been utilized to refine the location and strike of

some faults inferred from the aeromagnetic data, particularly Faults F1 and F10 (Figure 9), thereby providing more reliable geophysical evidence.

This study has yielded a wealth of lithological and structural information for the study area. The results have significantly enhanced the surface geological mapping by refining and enriching the understanding of strata, rock bodies, and structures, thereby compensating for the limitations of traditional surface surveys in the complex terrain of the study area. The litho-structural map generated from this study holds great potential for mineral exploration in the Nanpanjiang area. The utilization of airborne geophysical survey, as an efficient and cost-effective investigation tool, is particularly advantageous for areas characterized by intricate terrain and topography.

Author Contributions: Conceptualization, G.L. and Y.X.; methodology, G.L. and Y.L.; software, G.L. and Y.X.; investigation and validation, Y.X., S.W. and N.L.; writing—original draft preparation, G.L. and Y.L.; writing—review and editing, all participants; supervision, G.L. and Y.L. All authors have read and agreed to the published version of the manuscript.

Funding: This research was funded by the National Key Research and Development Program (grant number 2017YFC0602000 and 2016YFC0600209), and the China Geological Survey Project (grant number DD20160069-02).

Data Availability Statement: Data associated with this research are available and can be obtained by contacting the corresponding author.

Acknowledgments: The authors would like to thank the anonymous reviewers and editors for their valuable suggestions. We are also very grateful to the R & D team of the airborne geophysical survey system.

Conflicts of Interest: The authors declare no conflict of interest.

References

1. Lu, N.; Liao, G.; Xi, Y.; Zheng, H.; Ben, F.; Ding, Z.; Du, L. Application of Airborne Magnetic Survey in Deep Iron Ore Prospecting—A Case Study of Jinling Area in Shandong Province, China. *Minerals* **2021**, *11*, 1041. [[CrossRef](#)]
2. Youssef, M.A.S.; Elkhodary, S.T. Utilization of airborne gamma ray spectrometric data for geological mapping, radioactive mineral exploration and environmental monitoring of southeastern Aswan city, South Eastern Desert, Egypt. *Geophys. J. Int.* **2013**, *195*, 1689–1700. [[CrossRef](#)]
3. Wilson, G.; Damaske, D.; Möller, H.-D.; Tinto, K.; Jordan, T. The geological evolution of southern McMurdo Sound—New evidence from a high-resolution aeromagnetic survey. *Geophys. J. Int.* **2007**, *170*, 93–100. [[CrossRef](#)]
4. Zhdanov, M.S.; Alfouzan, F.A.; Cox, L.; Alotaibi, A.; Alyousif, M.; Sunwall, D.; Endo, M. Large-Scale 3D Modeling and Inversion of Multiphysics Airborne Geophysical Data: A Case Study from the Arabian Shield, Saudi Arabia. *Minerals* **2018**, *8*, 271. [[CrossRef](#)]
5. Saleh, S.; Salk, M.; Pamukçu, O. Estimating Curie Point Depth and Heat Flow Map for Northern Red Sea Rift of Egypt and Its Surroundings, from Aeromagnetic Data. *Pure Appl. Geophys.* **2013**, *170*, 863–885. [[CrossRef](#)]
6. Hussein, M.; Mickus, K.; Serpa, L.F. Curie Point Depth Estimates from Aeromagnetic Data from Death Valley and Surrounding Regions, California. *Pure Appl. Geophys.* **2013**, *170*, 617–632. [[CrossRef](#)]
7. Zhu, D.; Liu, T.; Yang, Y.; Chen, X.; Xiao, M. Geophysical interpretation of rock-controlling structure and concealed mass features in southeast Hubei province. *Earth Sci.* **2019**, *44*, 640–651.
8. Topien, R.M.; Moloto-A-Kenguemba, G.; Traore, M.; Rajendran, S.; Kouassi, B.R. Litho-structural mapping and structural evolution of the Bocaranga pluton, northwest Adamawa-Yadé domain, Central African Republic. *J. Afr. Earth Sci.* **2023**, *198*, 104793. [[CrossRef](#)]
9. Bakheit, A.A.; Abdel Aal, G.Z.; El-Haddad, A.E.; Ibrahim, M.A. Subsurface tectonic pattern and basement topography as interpreted from aeromagnetic data to the south of El-Dakhla Oasis, western desert, Egypt. *Arab. J. Geosci.* **2014**, *7*, 2165–2178. [[CrossRef](#)]
10. Anudu, G.K.; Stephenson, R.A.; Macdonald, D.I.M. Using high-resolution aeromagnetic data to recognise and map intra-sedimentary volcanic rocks and geological structures across the Cretaceous middle Benue Trough, Nigeria. *J. Afr. Earth Sci.* **2014**, *99*, 625–636. [[CrossRef](#)]
11. Sarma, B.S.P.; Chakravarthi, V. Delineation of concealed basement depression from aeromagnetic studies of Mahanadi Basin, East Coast of India. *Lead. Edge* **2011**, *30*, 854–857. [[CrossRef](#)]
12. Su, W.C.; Heinrich, C.A.; Pettke, T.; Zhang, X.C.; Hu, R.Z.; Xia, B. Sediment-hosted gold deposits in Guizhou, China: Products of wall-rock sulfidation by deep crustal fluids. *Econ. Geol.* **2009**, *104*, 73–93. [[CrossRef](#)]
13. Cline, J.S.; Muntean, J.L.; Gu, X.X. A comparison of Carlin-type gold deposits: Guizhou province, Golden Triangle, southwest China, and northern Nevada, USA. *Earth Sci. Front.* **2013**, *20*, 1–18.

14. Beamish, D.; White, J.C. Aeromagnetic data in the UK: A study of the information content of baseline and modern surveys across Anglesey, North Wales: Aeromagnetic data, Anglesey. *Geophys. J. Int.* **2011**, *184*, 171–190. [[CrossRef](#)]
15. Grauch, V.J.S.; Hudson, M.R. Guides to understanding the aeromagnetic expression of faults in sedimentary basins: Lessons learned from the central Rio Grande rift, New Mexico. *Geosphere* **2007**, *3*, 596. [[CrossRef](#)]
16. Grauch, V.J.S.; Bedrosian, P.A.; Drenth, B.J. Advancements in understanding the aeromagnetic expressions of basin-margin faults—An example from San Luis Basin, Colorado. *Lead. Edge* **2013**, *32*, 882–891. [[CrossRef](#)]
17. Toivonen, H. Airborne gamma spectrometry—towards integration of European operational capability. *Radiat. Prot. Dosim.* **2004**, *109*, 137–140. [[CrossRef](#)]
18. Carrier, F.; Bourdon, B.; Pili, É.; Truffert, C.; Wyns, R. Airborne gamma-ray spectrometry to quantify chemical erosion processes. *J. Geochem. Explor.* **2006**, *88*, 266–270. [[CrossRef](#)]
19. Butterweck, G.; Bucher, B.; Rybach, L.; Paschoa, A.S.; Steinhäusler, F. Airborne Gamma-Spectrometry in Switzerland. In *AIP Conference Proceedings*; American Institute of Physics: New York, NY, USA, 2008; Volume 1034, pp. 463–466. [[CrossRef](#)]
20. Sanderson, D.C.W.; Cresswell, A.J.; Hardeman, F.; Debauche, A. An airborne gamma-ray spectrometry survey of nuclear sites in Belgium. *J. Environ. Radioact.* **2004**, *72*, 213–224. [[CrossRef](#)]
21. Jayawardhana, P.M.; Sheard, S.N. The use of airborne gamma-ray spectrometry—A case study from the Mount Isa inlier, northwest Queensland, Australia. *Geophysics* **2000**, *65*, 1993–2000. [[CrossRef](#)]
22. Tourliere, B.; Perrin, J.; Leberre, P.; Pasquet, J. Use of airborne gamma-ray spectrometry for kaolin exploration. *J. Appl. Geophys.* **2003**, *53*, 91–102. [[CrossRef](#)]
23. Dilalos, S.; Alexopoulos, J.D. Regional Gravity Model of Greece Based on Satellite, Marine and Terrestrial Data. *Pure Appl. Geophys.* **2023**, *180*, 2807–2826. [[CrossRef](#)]
24. Farhi, W.; Boudella, A.; Saibi, H.; Bounif, M.O.A. Integration of magnetic, gravity, and well data in imaging subsurface geology in the Ksar Hirane region (Laghouat, Algeria). *J. Afr. Earth Sci.* **2016**, *124*, 63124. [[CrossRef](#)]
25. Smith, W.H.F.; Wessel, P. Gridding with continuous curvature splines in tension. *Geophysics* **1990**, *55*, 293–305. [[CrossRef](#)]
26. Subrahmanyam, V.; Swamy, K.V.; Raj, N. Basement configuration of KG offshore basin from magnetic anomalies. *J. Earth Syst. Sci.* **2016**, *125*, 663–668. [[CrossRef](#)]
27. Audet, P.; Gosselin, J.M. Curie depth estimation from magnetic anomaly data: A re-assessment using multitaper spectral analysis and Bayesian inference. *Geophys. J. Int.* **2019**, *218*, 494–507. [[CrossRef](#)]
28. Biedermann, A.R.; McEnroe, S.A. Effects of Magnetic Anisotropy on Total Magnetic Field Anomalies: AMS Effects on Magnetic Anomalies. *J. Geophys. Res. Solid Earth* **2017**, *122*, 8628–8644. [[CrossRef](#)]
29. Tampubolon, T.; Rahmatsyah; Harahap, M.A.T. Identification of magnetic anomalies in subsurface area of Sinabung mountain. *J. Phys. Conf. Ser.* **2018**, *1080*, 012041. [[CrossRef](#)]
30. Subba Rao, P.B.V.; Radhakrishna, M.; Haripriya, K.; Rao, B.S.; Chandrasekharam, D. Magnetic anomalies over the Andaman Islands and their geological significance. *J. Earth Syst. Sci.* **2016**, *125*, 359–368. [[CrossRef](#)]
31. Al-Heety, E.M.S.; Al-Mufarji, M.A.; Esho, L.H.A. Qualitative Interpretation of Gravity and Aeromagnetic Data in West of Tikrit City and Surroundings, Iraq. *Int. J. Geosci.* **2018**, *8*, 151–166. [[CrossRef](#)]
32. Gharti, H.N.; Tromp, J. Spectral-infinite-element simulations of magnetic anomalies. *Geophys. J. Int.* **2019**, *217*, 1656–1667. [[CrossRef](#)]
33. De Santis, A.; Pavón-Carrasco, F.J.; Ferraccioli, F.; Catalán, M.; Ishihara, T. Statistical analysis of the oceanic magnetic anomaly data. *Phys. Earth Planet. Inter.* **2018**, *284*, 28–35. [[CrossRef](#)]
34. Cai, J. Surface Magnetic Anomaly Triangulation Inversion. *Int. J. Geosci.* **2019**, *10*, 160–172. [[CrossRef](#)]
35. Idoko, C.M.; Conder, J.A.; Ferré, E.C.; Filiberto, J. The potential contribution to long wavelength magnetic anomalies from the lithospheric mantle. *Phys. Earth Planet. Inter.* **2019**, *292*, 21–28. [[CrossRef](#)]
36. Ekwok, S.E.; Akpan, A.E.; Achadu, O.-I.M.; Eze, O.E. Structural and lithological interpretation of aero-geophysical data in parts of the Lower Benue Trough and Obudu Plateau, southeast Nigeria. *Adv. Space Res.* **2021**, *68*, 2841–2854. [[CrossRef](#)]
37. Ba, M.H.; Jaffal, M.; Lo, K.; Youbi, N.; El Mokhtar Dahmada, M.; Ibouh, H.; Boumehdi, M.A.; Aïfa, T.; Amara, M.; Jessell, M.; et al. Mapping mafic dyke swarms, structural features, and hydrothermal alteration zones in Atar, Ahmeyim and Chami areas (Reguibat Shield, Northern Mauritania) using high-resolution aeromagnetic and gamma-ray spectrometry data. *J. Afr. Earth Sci.* **2020**, *163*, 103749. [[CrossRef](#)]
38. Ren, L.K. Analysis of Structural Styles and Kinematics Characteristics in Nanpanjiang Basin. *J. Kunming Univ. Sci. Technol.* **2012**, *37*, 1–4.
39. Liu, Y.H.; Liao, L.P. Discussion of Au, Sb Mineralization and Prospecting Direction in Southwest Guizhou. *Guizhou Geol.* **2015**, *32*, 163–180.
40. Gou, H.C. Preliminary research on tectonic background and material source area of turbidite deposit formation of Middle–Upper Triassic in Yunnan, Guizhou and Guangxi provinces. *Acta Sedimentol. Sin.* **1985**, *3*, 95–107.

Disclaimer/Publisher’s Note: The statements, opinions and data contained in all publications are solely those of the individual author(s) and contributor(s) and not of MDPI and/or the editor(s). MDPI and/or the editor(s) disclaim responsibility for any injury to people or property resulting from any ideas, methods, instructions or products referred to in the content.